3-D Radar Imaging Using Range Migration Techniques

Juan M. Lopez-Sanchez, *Student Member, IEEE* and Joaquim Fortuny-Guasch, *Member, IEEE*

***Abstract*—An imaging system with three-dimensional (3-D) capability can be implemented by using a stepped frequency radar which synthesizes a two-dimensional (2-D) planar aperture. A 3-D image can be formed by coherently integrating the backscatter data over the measured frequency band and the two spatial coordinates of the 2-D synthetic aperture. This paper presents a near-field 3-D synthetic aperture radar (SAR) imaging algorithm. This algorithm is an extension of the 2-D range migration algorithm (RMA). The presented formulation is justified by using the method of the stationary phase (MSP). Implementation aspects including the sampling criteria, resolutions, and computational complexity are assessed. The high computational efficiency and accurate image reconstruction of the algorithm are demonstrated both with numerical simulations and measurements using an outdoor linear SAR system.**

***Index Terms*—Near field, radar imaging, synthetic aperture radar.**

I. Introduction

SYNTHETIC aperture radar (SAR) is a well developed technique for producing high resolution images [1], [2]. There is a wide variety of imaging algorithms that have been used to reconstruct reflectivity images of a scene by using SAR techniques. A two-dimensional (2-D) reflectivity image can be formed by synthesizing a one-dimensional (1-D) aperture with a wide-band radar. Accordingly, a three-dimensional (3-D) reflectivity image is formed by synthesizing a 2-D aperture. As an example, typical geometries of the 2-D apertures that can be synthesized in an anechoic chamber are planar, spherical and cylindrical.

According to their working principle the existing radar imaging algorithms can be divided into three general groups [1]:

- *Polar Format Algorithm:* (also known as *Range-Doppler*) This algorithm was the first one to be developed and originates from optical signal processing. It is based on the polar nature of the frequency-domain backscatter data, works with motion compensation to a point and, as such, needs to be used under the far-field condition, requires an interpolation prior to the Fourier transform, and compensates only partially the range curvature. Both the 2-D and 3-D versions of this algorithm are of easy implementation and have been used extensively.

Manuscript received February 11, 1999; revised November 23, 1999.

J. M. Lopez-Sanchez is with the Departamento de Fisica, Escuela Politécnica Superior, Universidad de Alicante, 03080 Alicante, Spain.

J. Fortuny-Guasch is with the Space Applications Institute, Joint Research Centre of the European Commission, 21020 Ispra (Va), Italy (email: Joaquim.Fortuny@jrc.it).

Publisher Item Identifier S 0018-926X(00)04381-7.

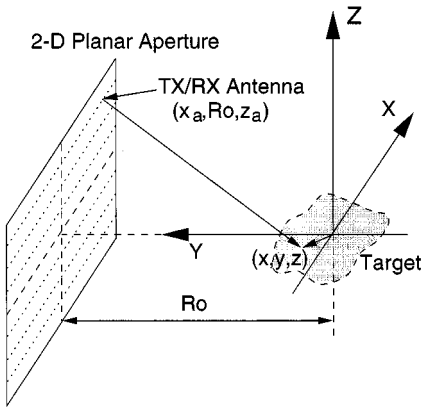

Fig. 1. Measurement and imaging geometry.

- *Range Migration Algorithm (RMA):* (In its 2-D version, it is also known as $\omega - k$ algorithm [3].) This algorithm originates from seismics engineering and geophysics. It works with motion compensation to a line, requires a one-dimensional (1-D) interpolation (known as Stolt interpolation [4]) and compensates completely the curvature of the wavefront. In the radar remote sensing domain it has only been used in its 2-D version. This is the first attempt known to the authors to formulate its 3-D version using a 2-D planar synthetic aperture. The RMA was firstly introduced to focus 2-D SAR data acquired from a space-borne platform in the strip map mode. Later it was adapted to be used in the spotlight mode [5]–[7]. Results showing that the RMA can also focus 2-D SAR data acquired in an anechoic chamber using the strip map mode are reported in [8]. Both the 2-D and 3-D versions of the RMA basically require a 1-D interpolator and fast Fourier transform (FFT) codes. As a result, their implementation on a massively parallel supercomputer becomes fairly straightforward [9].
- *Chirp Scaling Algorithm:* It has the original characteristic of not requiring any interpolation [10]. It works with motion compensation to a line and corrects approximately the range curvature. It is widely used to focus 2-D space- and airborne SAR data sets.

Note that the polar format algorithm cannot be used when the backscatter data are acquired on a planar aperture. Further, when the 2-D synthetic aperture is in the near-field zone of the target, the plane wave approximation is not valid and one needs to carefully correct for the wavefront curvature. This near-field correction is equally needed when the synthetic aperture is not planar. Examples of 2-D and 3-D inverse SAR (ISAR, i.e., with

0018–926X/00$10.00 © 2000 IEEE

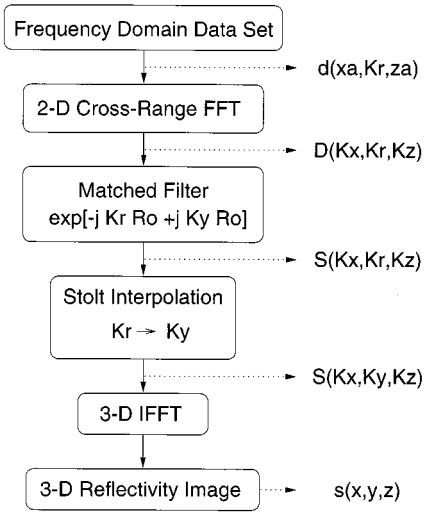

Fig. 2. Block diagram of the 3-D RMA.

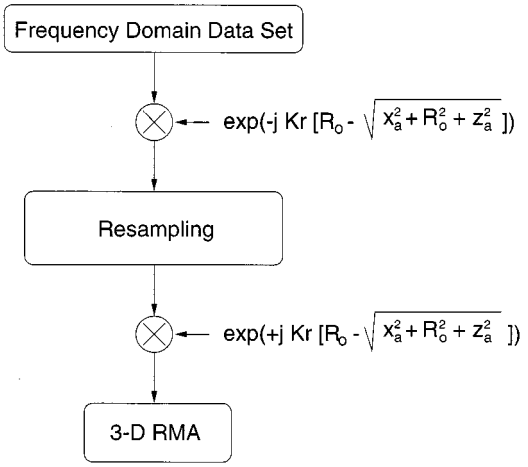

Fig. 3. Pre-processing of data sampled at the spotlight rate.

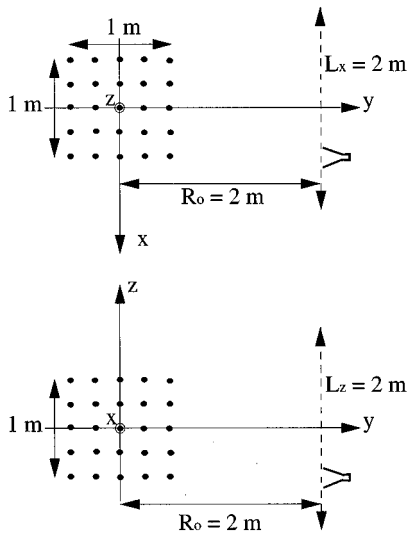

Fig. 4. Measurement setup used in the numerical simulation with the 3-D array of 125 point scatterers.

a target rotation in azimuth) algorithms that implement the near-field correction are presented in [11]–[14]. An example of near-field 2-D strip map SAR algorithm can be found in [15]. These algorithms are based on a one-dimensional (1-D) azimuth convolution between a near-field focusing function and the frequency-domain backscatter data, which precisely accounts for the wavefront curvature and the free-space propagation losses. This azimuth convolution is efficiently implemented by using FFT techniques. However, to get the complex radar reflectivity of a voxel in a 3-D image, two additional integrations over the frequency, and the incidence angle in elevation are required. These integrations cannot be implemented with FFT's and, therefore, the algorithm becomes computationally very costly.

The presented algorithm shows some similarities with the synthetic aperture focusing technique (SAFT) [16], [17]. This is a focusing technique well known in the field of ultrasonics which is based on a 3-D time domain backpropagation. However, as opposed to the presented technique, the SAFT is a time domain technique and does not make any use of neither the Stolt interpolator nor the method of stationay phase in its formulation. On the other hand, both algorithms require planar scan surfaces and can be applied under the near-field condition. The computational efficiency of these two techniques are supposed to be of the same order since both algorithms make an extensive use of FFT's. Another similar algorithm developed in the field of ultrasonics is the closed-time reversal cavity [18]–[20].

This paper presents a 3-D version of the RMA algorithm. The 2-D synthetic aperture is assumed to be planar and within the near-field zone of the target. As an input, the algorithm requires frequency domain backscatter data which can be acquired using a stepped frequency radar. Thus, resolution in the vertical and horizontal cross-range directions are given by the dimensions of the synthetic aperture, whereas resolution in ground-range is provided by the synthesized frequency bandwidth. The frequency-domain data is preferred because the RMA algorithm works in the frequency wavenumber domain. Note that the focusing of time-domain data sets acquired with a pulsed system would become straightforward by simply applying a Fourier transform.

The RMA algorithm, as all SAR algorithms, is based on a linearization of the electromagnetic wave scattering problem. This means that the interaction between the scatterers present in the scene is totally neglected. This approximation is widely used in the field of radar imaging since appropriate 3-D nonlinear imaging algorithms dealing with the inverse scattering problem have not yet been developed.

The measurements are supposed to be fully controlled and therefore factors such as irregular sample spacing, platform position errors and mitigation of RFI have not been investigated. The objective of this work is to develop a rapid and efficient 3-D imaging technique for the identification and characterization of radar reflectivity components of complex objects.

This paper is organized as follows. Section II presents the formulation of the 3-D RMA which has been derived by using the method of stationary phase (MSP) [21], as suggested in [1]

for the 2-D RMA. A description of the algorithm implementation and the different data processing steps is given in Section III. Section IV deals with some practical aspects on the actual implementation of the algorithm, the required sampling criteria and the resulting resolutions. Section V-A presents the numerical simulations that have been carried out for testing this algorithm. Moreover, experimental results showing the validity of this imaging method are shown in Section V-B. The conclusions are summarized in Section VI. Appendixes A and B deal with two alternative derivations of the same formulation of the RMA using the MSP.

II. Formulation of the 3-D RMA

Consider the measurement setup shown in Fig. 1. A stepped frequency radar illuminates a target with a CW of frequency f. The antenna is positioned at (x_a, R_o, z_a) and synthesizes a rectangular aperture on a plane parallel to the XZ at a distance R_o. The measurement points form a rectangular grid with spacings Δx_a and Δz_a in the horizontal and vertical cross-range directions, respectively. At each antenna position the synthesized frequency bandwidth is B. Thus, the acquired backscatter data $d(x_a, f, z_a)$ are function of two spatial coordinates and the working frequency. The frequency variable is directly related with the two-way frequency wavenumber $k_r = 4\pi f/c$. Consequently, the measurement data can also be denoted as $d(x_a, k_r, z_a)$.

Assuming that there is a point scatterer located at (x, y, z) with reflectivity $s(x, y, z)$, then the measured backscatter is

$$d(x_a, k_r, z_a) = s(x, y, z) \exp[+jk_r R_o] \exp[-jk_r R] \quad (1)$$

where R is the range to the point scatterer, i.e.,

$$R = \sqrt{(x - x_a)^2 + (y - R_o)^2 + (z - z_a)^2}. \quad (2)$$

The first exponential in (1) establishes the phase reference at the origin of the coordinate system which is at a distance R_o from the aperture. In the 2-D RMA this reference is a line parallel to the linear aperture. The second exponential simply accounts for the phase history associated with the point scatterer. Note that for the sake of simplicity, the losses due to the free-space propagation and the antenna pattern are not considered here.

From (1), the 3-D radar reflectivity map associated with a distributed target can be expressed as

$$s(x, y, z) = \iint\limits_{A, k_r} d(x_a, k_r, z_a) \exp[-jk_r R_o] \times \exp[jk_r \sqrt{(x - x_a)^2 + (y - R_o)^2 + (z - z_a)^2}] \times dx_a \, dz_a \, dk_r \quad (3)$$

where A denotes the surface of the synthetic aperture. Equation (3) can be reformulated in order to show that the focusing algorithm can be simply implemented by means of a 2-D convolution and a frequency integration

$$s(x, y, z) = \int_{k_r} \exp[-jk_r R_o] \iint\limits_{A} d(x_a, k_r, z_a) \times \exp[jk_r \sqrt{(x - x_a)^2 + (y - R_o)^2 + (z - z_a)^2}] \times dx_a \, dz_a \, dk_r. \quad (4)$$

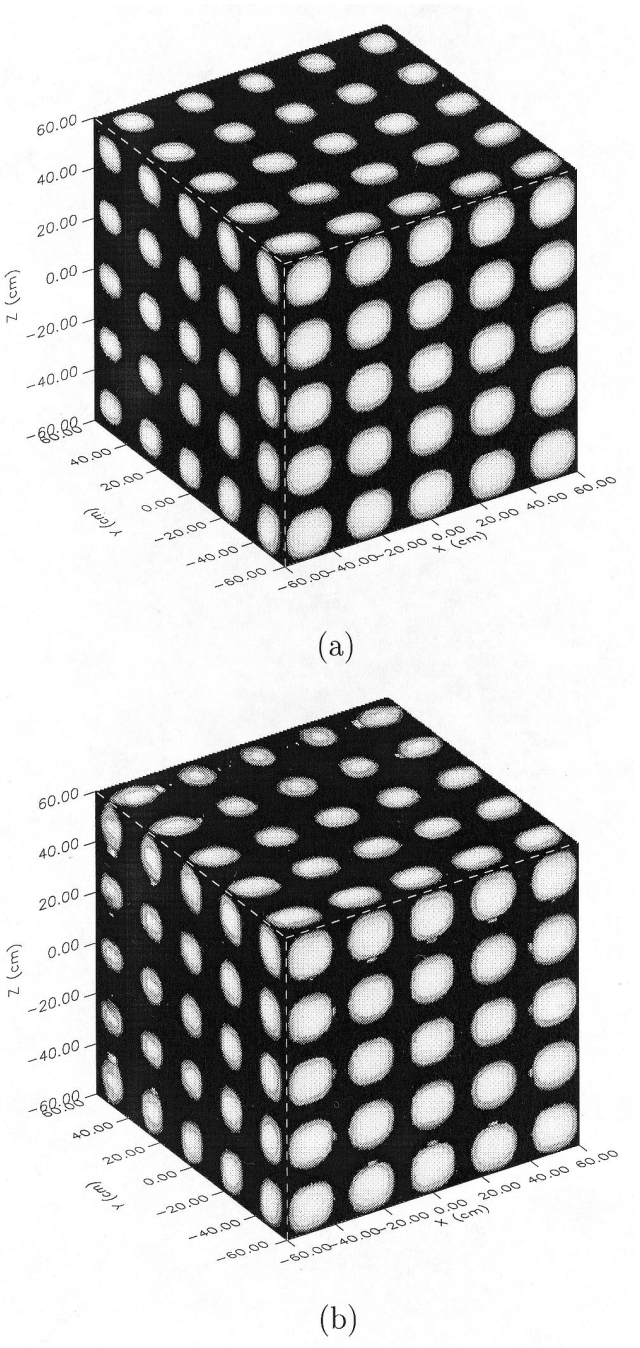

Fig. 5. Projections of the 3-D SAR image onto the XY, XZ and YZ planes. Simulation of 125 point scatterers. Parameters: $R_o = L_x = L_z = 2$ m, $f =$ 2–6 GHz, $\delta x = \delta y = \delta z = 3.75$ cm, $\Delta f = 100$ MHz, $\Delta x_a = \Delta z_a = 4$ cm, Displayed dynamic range is 50 dB. (a) Original RMA (b) RMA-FReD.

Note that (3) is a solution of the linearized inverse scattering problem and as such it only holds under the first-order Born approximation. Here it is also assumed that the backscattered fields will vanish at the boundaries of the aperture. This boundary condition is satisfied by simply applying a 2-D weighting function or window prior to the focusing, something which is a common practice in any imaging algorithm.

The 2-D convolution in the aperture coordinates (x_a, z_a) can be computed in the Fourier domain as a complex product if the following 2-D Fourier transform (FT) were known:

$$E(k_x,k_z) = \iint \exp[jk_r\sqrt{x^2+(y-R_o)^2+z^2}] \times \exp[-jk_x x - jk_z z]\,dx\,dz. \quad (5)$$

These kind of integrals, under certain conditions, can be evaluated analytically by using the method of stationary phase (MSP) [21]. The MSP states that the main contribution to the integral comes from points with stationary phase (nulls of the phase derivative) and gives an asymptotic expansion for the integral. The evaluation of the 2-D integral in (5) by means of the MSP results in (see Appendixes A and B):

$$E(k_x,k_z) \simeq \frac{2\pi k_r}{jk_y^2}\exp[-jk_y(y-R_o)] \quad (6)$$

where $k_y = \sqrt{k_r^2-k_x^2-k_z^2}$. Replacing the 2-D FT by its asymptotic expansion in (4), the 3-D reflectivity image is given by

$$s(x,y,z) \simeq \iiint_K D(k_x,k_r,k_z)\frac{2\pi k_r}{jk_y^2}\exp[-jk_r R_o] \times \exp[j(k_x x + k_z z - k_y(y-R_o)]\,dk_x\,dk_r\,dk_z \quad (7)$$

where $D(k_x,k_r,k_z)$ is the 2-D horizontal/vertical cross-range FFT of the frequency-domain backscatter data. The last exponential term takes the form of the Fourier kernel in a 3-D inverse FFT (IFFT). However, prior to this 3-D IFFT, the wavenumber domain backscatter data need to be resampled uniformly in k_y. Then, by substituting the frequency wavenumber variable k_r by k_y, the reflectivity image takes the form

$$s(x,y,z) \simeq \iiint_K D(k_x,k_y,k_z)\frac{2\pi}{jk_y}\exp[-j(k_r-k_y)R_o] \times \exp[jk_x x + jk_z z - jk_y y]\,dk_x\,dk_y\,dk_z. \quad (8)$$

Note that the amplitude term has been modified due to the change of variables $(k_r \rightarrow k_y)$. Equation (8) indicates that reflectivity image can be simply obtained through an 3-D IFFT of the product of the resampled wavenumber domain backscatter data by a complex exponential (also known as matched filter).

III. Algorithm Implementation

This section deals with the practical implementation of the 3-D RMA. From (8), the image reconstruction process can be naturally split into four sequential steps (see Fig. 2), namely: a 2-D cross-range FFT, matched filtering, Stolt interpolation, and a 3-D IFTT. The first and the last steps are obvious and will not be discussed here. However, the matched filter and the Stolt interpolation deserve special treatment.

The matched filter is necessary to introduce a motion compensation to the wavenumber domain backscatter data. This motion compensation corrects for the wavefront curvature of all scatterers at the same ground range as the scene center (i.e., the origin of the coordinates system). In the next step, the residual range curvature of all scatterers will be removed. The phase associated with the matched filter is space-invariant and depends only on the range to the scene center R_o, the frequency and the cross-range wavenumbers. It is given by

$$\Phi_{\mathrm{MF}}(k_x,k_r,k_z) = -k_r R_o + k_y R_o = -k_r R_o + \sqrt{k_r^2-k_x^2-k_z^2}R_o \quad (9)$$

where the identity

$$k_y = \sqrt{k_r^2-k_x^2-k_z^2} \quad (10)$$

is known as the Stolt transformation [4]. Note that in (10), k_y must be real and, therefore, the region in the wavenumber do-

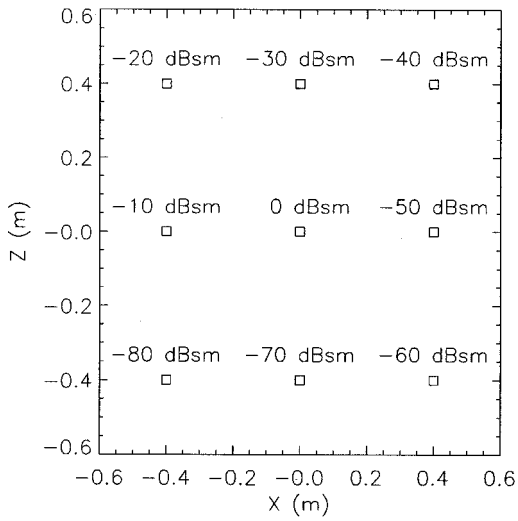

(a)

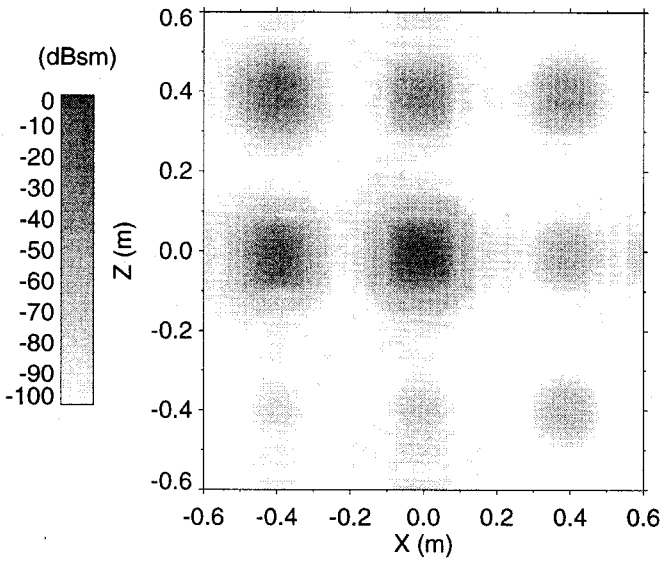

(b)

Fig. 6. Target modeled to evaluate the dynamic range. (a) Sketch of the target. (b) Slice of the reflectivity image.

main where the asymptotic expansion of the MSP is valid reduces to

$$k_r^2 \geq k_x^2 + k_z^2. \tag{11}$$

The field modes which satisfy this inequality are the so-called propagating modes, whereas those which do not propagate are the evanescent modes. The amplitude of the evanescent modes is affected by an exponential factor which rapidly vanishes with an increasing distance to the aperture $(y - R_o)$. In the formulation presented here, it is assumed that (11) is satisfied. In practice, the data points in the wavenumber domain outside the region defined by (11) will be discarded by applying a mask prior to the matched filter.

The third step performed in the 3-D RMA is the Stolt interpolation. This interpolation compensates the range curvature of all scatterers by an appropriate warping of the wavenumber domain backscatter data. After the matched filter the transformed data continue being equally spaced in frequency and, therefore, in the k_r variable. In order to prepare the data for the last 3-D IFT, the next step consists of a change of variables defined by the Stolt transformation, which can be implemented as a 1-D interpolation. As a result, the wavenumber domain backscatter data will be uniformly sampled in the k_y domain. In the present implementation of the algorithm, the sampling frequency is increased to be highly above the Nyquist limit, then a Lagrange interpolation preceded by a frequency downconversion is applied.

Once the Stolt interpolation is performed, the wavenumber domain backscatter data have to be multiplied by the amplitude terms due to change of variable and the asymptotic expansion of (8). Then, the 3-D reflectivity image is obtained by simply applying a 3-D IFFT.

IV. Resolution and Sampling Criteria

A. Resolutions

The resolutions in the resulting 3-D reflectivity image depend on the frequency bandwidth, the center frequency and the dimensions of the synthetic aperture. The ground-range resolution is usually expressed as

$$\delta_y \simeq \frac{c}{2B} \tag{12}$$

where B is the frequency bandwidth. The horizontal and vertical cross-range resolutions are

$$\delta_x \simeq \frac{\lambda_c R_o}{2L_x} = \frac{cR_o}{2f_c L_x} \tag{13}$$

$$\delta_z \simeq \frac{\lambda_c R_o}{2L_z} = \frac{cR_o}{2f_c L_z} \tag{14}$$

where L_x and L_z are the lengths of the 2-D synthetic aperture and λ_c is the wavelength at the center frequency f_c.

In practice, the frequency-domain backscatter data are windowed to lower the sidelobes in the imagery and, as a result, the final resolutions are usually slightly poorer than those given by the above formulas.

TABLE I
Measured Reflectivity Values for the Target in Fig. 6

Nominal	Measured RCS (dBsm)		
RCS (dBsm)	$y = -0.4$ m	$y = 0.0$ m	$y = 0.4$ m
0	−0.08	−0.10	−0.12
−10	−10.39	−10.53	−10.71
−20	−20.71	−20.95	−21.30
−40	−40.69	−40.94	−41.30
−60	−60.75	−60.99	−61.31
−80	−79.82	−80.45	−81.07

B. Sampling Criteria

Assuming that the target is confined within a rectangular box of dimensions $D_x \times D_y \times D_z$ centered at the origin of the coordinates, the required sampling steps in the measurement to satisfy the Nyquist criterion are given by

$$\Delta_f \leq \frac{c}{2D_y} \tag{15}$$

$$\Delta_{x_a} \leq \frac{\lambda_{\min}}{2} \frac{\sqrt{(L_x + D_x)^2/4 + R_o^2}}{L_x + D_x} \tag{16}$$

$$\Delta_{z_a} \leq \frac{\lambda_{\min}}{2} \frac{\sqrt{(L_z + D_z)^2/4 + R_o^2}}{L_z + D_z} \tag{17}$$

where $\lambda_{\min}$ is the wavelength at the maximum working frequency.

The sampling intervals given by (16) and (17) are the usual ones in strip map SAR. The measurement points on the aperture require a minimum spacing in order to sample adequately the phase history associated with all the scatterers after the matched filter. As a result, the sampling frequencies in a strip map SAR are much higher than those in a spotlight configuration. Note that in a spotlight SAR the minimum cross-range spacing only depends on the target size and the distance to the aperture, but not on the aperture size as in a strip map SAR. Consequently, strip map SAR measurements will have associated larger data volumes and longer measurement times.

Running a strip map SAR measurement at the spotlight SAR sampling frequency will introduce aliasing in the acquired data set. However, the origin of the aliasing is known and can be eliminated by introducing a deterministic phase correction term. The phase correction term which needs to be applied is as follows:

$$\mathrm{HF}(x_a, k_r, z_a) = \exp\left[jk_r\left(R_o - \sqrt{x_a^2 + R_o^2 + z_a^2}\right)\right]. \tag{18}$$

After applying the correction term, the aliasing has been eliminated, the sampling rate can be increased in order to satisfy (16) and (17). Then a second phase correction, complex conjugate of the first one, is applied to restore the original phase reference in the data. The main advantage of this procedure is the

reduction of both the data volume and the measurement times. From the viewpoint of the RMA, this pre-processing is completely transparent and does not have any side effect. Note that the 3-D RMA maintains the same requirements in terms of internal memory and computational load. The flowchart associated with this pre-processing is shown in Fig. 3. The resulting cross-range sampling intervals (i.e., the ones used in a spotlight SAR) are

$$\Delta_{x_a} \leq \frac{\lambda_{\min} R_o}{2\sqrt{D_x^2 + D_y^2}} \tag{19}$$

$$\Delta_{z_a} \leq \frac{\lambda_{\min} R_o}{2\sqrt{D_z^2 + D_y^2}}. \tag{20}$$

In [6] and [7], an alternative technique to process strip map data at the spotlight sampling frequency is presented. This technique, named fequency domain replication and downsampling (RMA-FReD) in [7], has been used with airborne data. With this technique, the blurred replicas due to the aliasing fall ideally out of the scene and the final image presents a slightly lower signal-to-background-ratio and a wider impulse response. If this minor degradation in the image quality is accepted, one can use the RMA-FReD as a quicklook processor. Note that with the RMA-FReD, the data volume to be processed is by far smaller than that in the conventional RMA. In the next section, the results obtained with these two processors are compared.

V. Results

The high computational efficiency and accurate image reconstruction of the algorithm are demonstrated both with numerical simulations and measurements using an outdoor linear SAR system. The code of the algorithm has been implemented in the C programming language. The computer used to focus the data is a high-performance Sun Ultra-Sparc workstation, equipped with a 64 bit CPU and 128 MByte of RAM. What follows is the description of the measurement setups and the results on simulated and real data sets.

A. Numerical Simulations

Fig. 4 shows a sketch of the target used in the first numerical simulation. The target consists of a 3-D array of $5 \times 5 \times 5$ point scatterers uniformly distributed within a box of side 1 m. All scatterers have the same radar cross section (RCS): 0 dBsm. A TX/RX antenna synthesizes a planar aperture of 2 m $\times$ 2 m located at $R_o = 2$ m from the target center. The number of measurement points is 51, spaced 4 cm, both in the horizontal and vertical cross-range directions. These sampling intervals have been selected according to the spotlight criterion. The resulting sampling intervals without the proposed pre-processing would be 2 cm. The frequency ranges from 2 to 6 GHz, sampling a total of 41 points with a step of 100 MHz. According to these parameters the theoretical resolution is 3.75 cm along the three main axes.

Two 3-D reflectivity images have been reconstructed using the RMA and the RMA-FReD, respectively. The reflectivity image has been reconstructed in a cube of side 1.2 m, with a total of 61 voxel in each dimension. Fig. 5 shows the projection of the images onto the three main planes. A Kaiser–Bessel $(\alpha = 2)$ window has been applied along the dimensions of the frequency-domain data set [22]. The dynamic range shown in the image is 50 dB. Both results show a slight dependence on the ground-range coordinate (y). This effect is common in near field measurements since the algorithm does not focus with the same accuracy close and distant points. Anyway, the quality of the reconstructed image is quite satisfactory and, moreover, the processing time is very short. In the RMA case the processing time was 3 min and 40 s, requiring about 13 MB of RAM. The image obtained with the RMA-FReD processor shows some inaccuracies which show reflectivity values below -30 dBsm. These imperfections are present in the near range zone because this area introduces the highest spatial frequencies. However, with this processor, the processing time took only 1 min, requiring only 3 Mb of RAM.

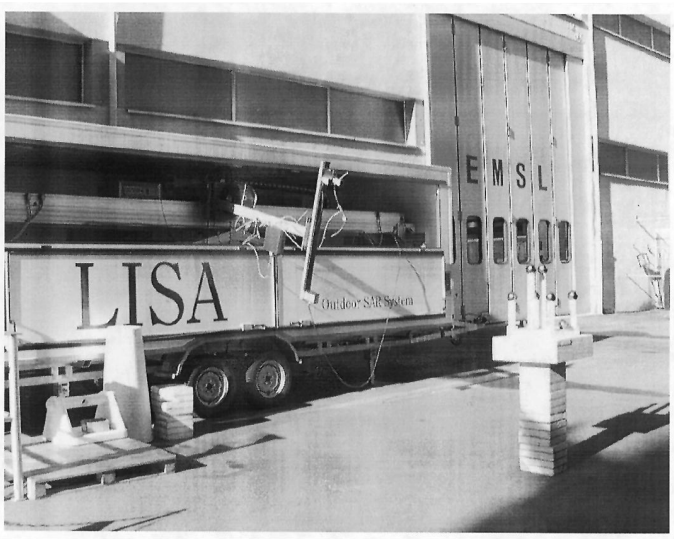

Fig. 7. Photograph of the experiment setup with LISA.

The second simulation is intended to estimate the dynamic range of the 3-D RMA processor. The target is similar to the one used in the previous simulation. It consists of three parallel planes spaced 40 cm, where nine scatterers have been uniformly distributed as shown in Fig. 6(a). The reflectivities now vary and range from 0 to -80 dBsm. The measurement setup is identical to that of the first simulation. The reflectivity image has been reconstructed using the 3-D RMA. Fig. 6(b) shows the slice corresponding to a vertical plane parallel to the aperture at $y = 0$. The dynamic range of this image is 100 dB. As in the previous results, a Kaiser–Bessel $(\alpha = 2)$ window has been applied. It is seen that the dynamic range of the imaging algorithm is better than 80 dB. In practice, the dynamic range will be limited by the presence of noise in the system. Table I compares the reconstructed values of the reflectivity with the actual ones. The maximum error is in the order of 1.5 dB.

B. Experimental Results

The presented 3-D imaging algorithm has been validated experimentally by using an outdoor linear SAR system (LISA). This system is based on a stepped frequency radar which

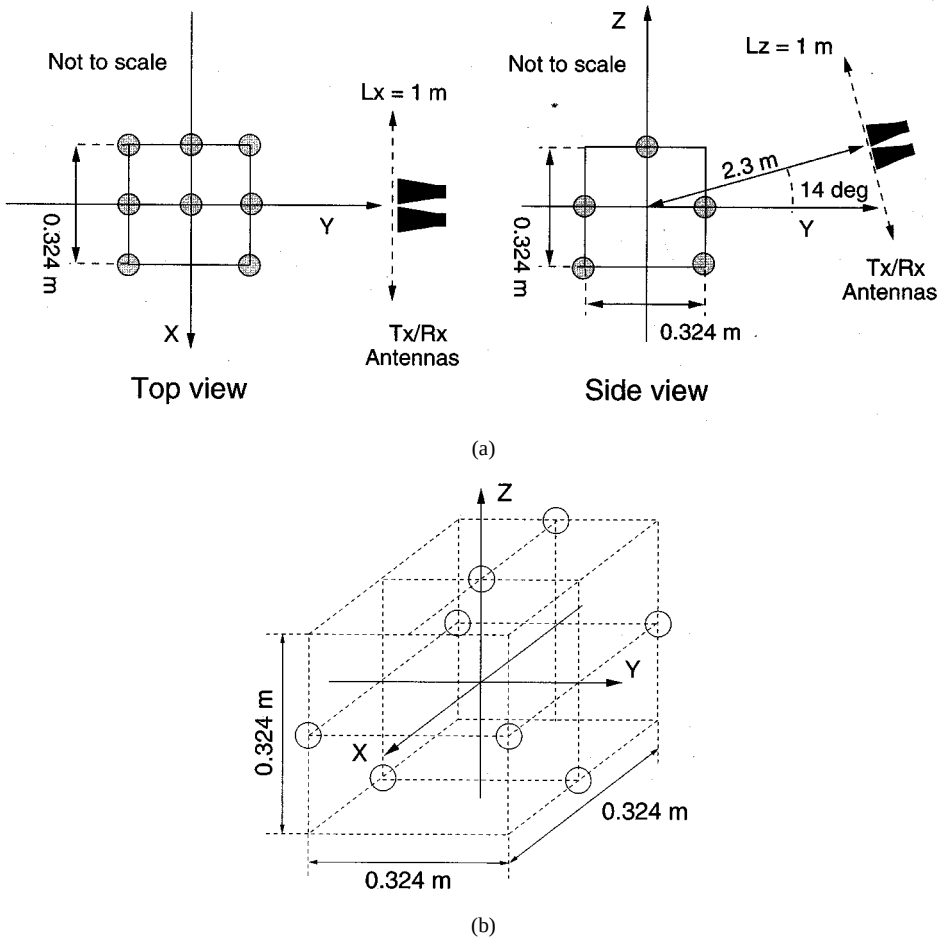

Fig. 8. (a) Arrangement of the measurement setup used in the experimental validation with a 3-D array of eight spheres. (b) Sketch of the target.

is equipped with a 2-D positioning system. The maximum aperture dimensions are at present limited to 5 and 1 m in the horizontal and vertical cross-range directions, respectively. The positioning accuracy is better that 0.1 mm. The frequency range is basically limited by the type of antennas being used. The system performs quasi-monostatic measurements using two closely spaced horn antennas.

Fig. 7 shows the measurement setup used in the experimental validation. The target consists of a 3-D arrangement of eight metallic spheres of diameter 7.62 cm, positioned as shown in Fig. 8. The dimensions of the 2-D synthetic aperture are 1 m $\times$ 1 m, with a total of 41 measurement points equally spaced in the horizontal and vertical directions. The backscattered fields in the horizontal (HH) polarization were acquired at 401 frequency points spaced 5 MHz within the frequency range 15.5–17.5 GHz. The range, from the center of the aperture to the center of the target, was 2.3 m. The plane of the aperture was tilted 14 degrees from the vertical. The expected resolutions should be 2 cm in the horizontal (X) and vertical (Z) cross-range directions, and 7.5 cm in the ground-range (Y) direction.

The measurement time required in this experiment was approximately 2 h. A 3-D reflectivity image confined in a box of side 60 cm with 61 voxel in each dimension has been reconstructed. The processing time was 1 min and 43 s. Fig. 9 shows some slices out of the reconstructed 3-D image: three slices at different ground-range ($y = -16, 0, +16$ cm) and cross-range ($x = -16, 0, +16$ cm) positions. The displayed dynamic range is 20 dB. As expected, the reflectivity at the positions of the spheres is about -23.4 dBsm, corresponding to the RCS given by the physical optics approximation. The measured spatial resolutions are in agreement with the expected ones. Note that the reflectivity peaks of the spheres closer to the antennas are narrower because the effective synthetic aperture is larger in the near range. On the other hand, the spheres have a diameter of about four wavelengths and, therefore, they are not ideal point scatterers. As a result, a minor degradation or defocusing must be expected.

VI. Conclusion

A new near-field three-dimensional (3-D) radar imaging algorithm has been presented. It is an extension of the two-dimensional (2-D) RMA. The formulation has been justified by using of the method of stationary phase. Implementation aspects including the sampling criteria, resolutions and computational complexity have been assessed. The numerical simulations have shown the efficiency of the algorithm, which can be simply implemented by using FFT codes and a 1-D Lagrange interpolator. An important feature of the proposed processing scheme is that by applying a phase correction term, strip-map

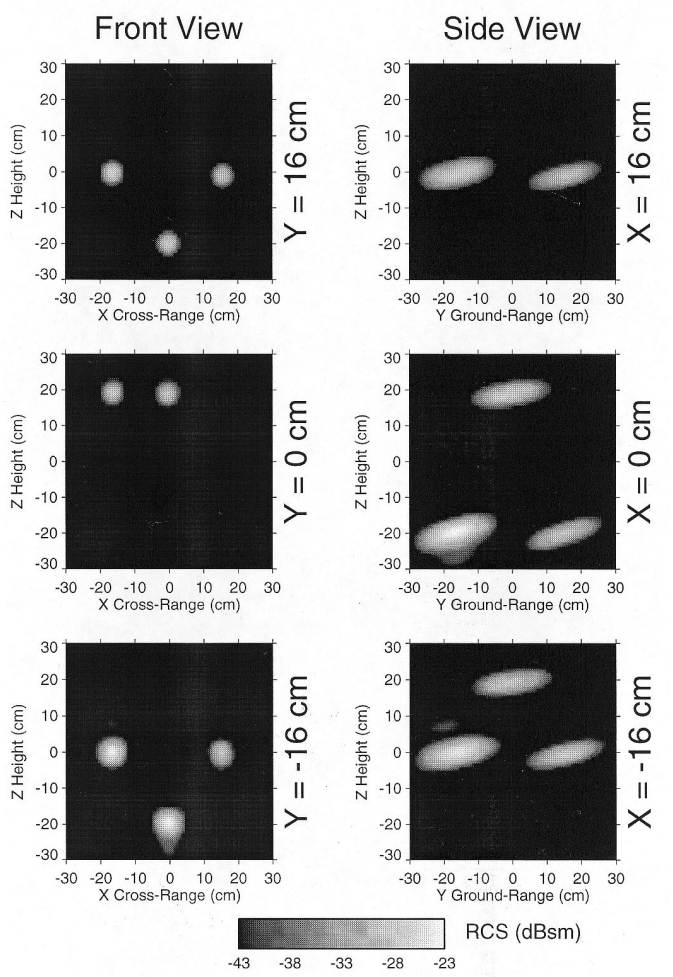

Fig. 9. Slices of the reconstructed 3-D image with the eight spheres measured by LISA.

SAR measurements can be performed at the spotlight SAR sampling rate without introducing any degradation in the imagery. The quality of the focused images is very high and in the numerical simulations it has shown to reach dynamic ranges better than 80 dB. The algorithm has been also validated experimentally using a vehicle-mounted SAR system. These results have shown the high performance of the algorithm working with an experimental data set.

The development of a new algorithm especially tailored for cylindrical and spherical apertures is in progress. This algorithm will be used in combination with the 3-D RMA algorithm.

Appendix A
Application of Stationary Phase Method

The 2-D Fourier transform in (5) can be evaluated asymptotically by using the method of stationary phase (MSP) [21]. This method provides an analytical solution to integrals of the form

$$N(k) = \iint_R f(x,y)\,\exp[jk\mu(x,y)]\,dx\,dy \tag{21}$$

where R is a region in the $X-Y$ plane, and $\mu(x,y)$ is a function assumed to be twice-continuously differentiable in R. The asymptotic evaluation of $N(k)$ for large k can be obtained by looking for the zeros of the first derivative of the argument of the exponential term. The major contribution to the integral in (21) comes from a small neighborhood near the points where the two first derivatives of $\mu(x,y)$ vanish. These points are known as points of stationary phase.

In the RMA, the objective is to evaluate the integral

$$E(k_x,k_z) = \iint \exp[jk_r\sqrt{x^2+(y-R_o)^2+z^2}] \times \exp[-jk_x x - jk_z z]\,dx\,dz. \tag{22}$$

The phase of the exponential term is given by

$$\Phi(x,z) = k\mu(x,z) = k_r R - k_x x - k_z z \tag{23}$$

$$R = \sqrt{x^2+(y-R_o)^2+z^2}. \tag{24}$$

If there is only one point of stationary phase, the resulting asymptotic expansion of $E(k_x,k_z)$ is

$$E(k_x,k_z) \simeq \frac{j2\pi}{\sqrt{\Phi_{xx}\Phi_{zz}-\Phi_{xz}^2}}\exp[j\Phi(x_0,z_0)] \tag{25}$$

where Φ_{xx},Φ_{zz} and Φ_{xz} denote the second partial derivatives of $\Phi(x,z)$ evaluated at the stationary point. The stationary point (x_0,z_0) is the point where the phase $\Phi(x,z)$ takes an extreme value, i.e.,

$$\left.\frac{\partial\Phi}{\partial x}\right|_{(x_0,z_0)} = 0 \tag{26}$$

$$\left.\frac{\partial\Phi}{\partial z}\right|_{(x_0,z_0)} = 0 \tag{27}$$

and, at the same time, it is assumed that

$$\Phi_{xx}\Phi_{zz}-\Phi_{xz}^2 \neq 0 \quad \text{and} \quad \Phi_{zz}\neq 0. \tag{28}$$

The first derivatives of the phase function are

$$\Phi_x(x,z) = \frac{\partial\Phi}{\partial x} = -k_x + \frac{k_r x}{R} \tag{29}$$

$$\Phi_z(x,z) = \frac{\partial\Phi}{\partial z} = -k_z + \frac{k_r z}{R}. \tag{30}$$

There is only one point were both first derivatives vanish simultaneously

$$x_0 = -\frac{k_x(y-R_o)}{\sqrt{k_r^2-k_x^2-k_z^2}} \tag{31}$$

$$z_0 = -\frac{k_z(y-R_o)}{\sqrt{k_r^2-k_x^2-k_z^2}} \tag{32}$$

where it has been assumed that $y < R_o$ (i.e., the reflectivity image is calculated in a box centered at the origin of the coordinates system which does not enclose the synthetic aperture). The asymptotic expansion provided by the MSP is only valid if

the coordinates (x_0, z_0) are both real, therefore, the frequency wavenumber must satisfy the following inequality:

$$k_r^2 \geq k_x^2 + k_z^2. \tag{33}$$

The second partial derivatives evaluated at the stationary point yield

$$\Phi_{xx}(x_0, z_0) = -\frac{(k_r^2 - k_x^2)\sqrt{k_r^2 - k_x^2 - k_z^2}}{k_r^2(y - R_o)} \tag{34}$$

$$\Phi_{zz}(x_0, z_0) = -\frac{(k_r^2 - k_z^2)\sqrt{k_r^2 - k_x^2 - k_z^2}}{k_r^2(y - R_o)} \tag{35}$$

$$\Phi_{xz}(x_0, z_0) = \frac{k_x k_z \sqrt{k_r^2 - k_x^2 - k_z^2}}{k_r^2(y - R_o)}. \tag{36}$$

Moreover, the function $\Phi(x, y)$ evaluated at the stationary point is

$$\Phi(x_0, z_0) = -\sqrt{k_r^2 - k_x^2 - k_z^2}(y - R_o). \tag{37}$$

Finally, substituting (34)–(37) into (25), the resulting expression for the 2-D Fourier transform of (22) is

$$E(k_x, k_z) \simeq \frac{2\pi(y - R_o)k_r}{jk_y^2} \exp[-jk_y(y - R_o)] \tag{38}$$

where $k_y = \sqrt{k_r^2 - k_x^2 - k_z^2}$.

Note that the factor $(y - R_o)$ in (38) cannot be applied in practice because the ground-range variable y is not defined in the wavenumber domain. This is an amplitude factor and as such has a negligible effect on the quality of the final image. Thus, the asymptotic expansion to be used in the RMA becomes

$$E(k_x, k_z) \simeq \frac{2\pi k_r}{jk_y^2} \exp[-jk_y(y - R_o)]. \tag{39}$$

Appendix B
Alternative Interpretation of RMA

The main objective of the RMA is to reconstruct the reflectivity image by using a 3-D inverse Fourier transform in the last step, i.e.,

$$s(x, y, z) = \iiint_K S(k_x, k_y, k_z) \times \exp[jk_x x + jk_y y + jk_z z]\, dk_x\, dk_y\, dk_z. \tag{40}$$

Since $s(x, y, z)$ and $S(k_x, k_y, k_z)$ form a Fourier transform pair, we have that

$$S(k_x, k_y, k_z) = \iiint_V s(x, y, z) \times \exp[-jk_x x - jk_y y - jk_z z]\, dx\, dy\, dz \tag{41}$$

where V denotes the volume occupied by the target.

The frequency-domain backscatter data can be expressed as an integral of the reflectivity function weighted by an exponential phase term $\exp[-jk_r R]$

$$d(x_a, k_r, z_a) = \iiint_V s(x, y, z) \exp[+jk_r R_o] \times \exp[-jk_r R]\, dx\, dy\, dz \tag{42}$$

where the first exponential establishes a phase reference (see Section II) and R is the range to the point at (x, y, z), i.e.,

$$R = \sqrt{(x - x_a)^2 + (y - R_o)^2 + (z - z_a)^2}. \tag{43}$$

The RMA performs a cross-range 2-D FT on the acquired data over the aperture A. It is expressed as

$$D(k_x, k_r, k_z) = \iint_A d(x_a, k_r, z_a) \times \exp[-jk_x x_a - jk_z z_a]\, dx_a\, dz_a. \tag{44}$$

By substituting (42) into (44) and evaluating the resulting surface integral by means of the MSP, the final result (omitting the matched filter term) is

$$D(k_x, k_r, k_z) = \iiint_V s(x, y, z) \times \exp[-jk_x x - jk_y y - jk_z z]\, dx\, dy\, dz \tag{45}$$

which has the same form as (41) after the Stolt transformation $(k_r \rightarrow k_y)$. This shows that the 3-D FFT of the reflectivity image $D(k_x, k_r, k_z)$ is directly related to the 3-D FFT of the measured data $S(k_x, k_y, k_z)$, thus, further justifying the presented 3-D RMA algorithm.

Acknowledgment

The authors would like to thank D. Tarchi and D. Leva for their support in performing the measurements and providing the experimental data. Special thanks are also due to Dr. A. J. Sieber for his support of this work.

References

[1] W. G. Carrara, R. S. Goodman, and R. M. Majewski, *Spotlight Synthetic Aperture Radar. Signal Processing Algorithms*. Boston, MA: Artech House, 1995.

[2] D. A. Ausherman, A. Kozma, J. L. Walker, H. M. Jones, and E. C. Poggio, "Developments in radar imaging," *IEEE Trans. Aerosp. Electron. Syst.*, vol. 20, pp. 363–400, July 1984.

[3] C. Cafforio, C. Prati, and E. Rocca, "SAR data focusing using seismic migration techniques," *IEEE Trans. Aerosp. Electron. Syst.*, vol. 27, pp. 194–207, Mar. 1991.

[4] R. Stolt, "Migration by Fourier transform techniques," *Geophys.*, no. 43, pp. 49–76, 1978.

[5] C. Prati, A. M. Guarnieri, and F. Rocca, "Spot mode SAR focusing with the $\omega - k$ technique," in *Proc. IEEE Int. Geosci. Remote Sensing Symp. (IGARSS)*, Helsinki, Finland, June 1991, pp. 631–634.

[6] C. Prati and F. Rocca, "Focusing SAR data with time-varying Doppler centroid," *IEEE Trans. Geosci. Remote Sensing*, vol. 30, pp. 550–559, May 1992.

[7] A. Golden Jr., S. C. Wei, K. K. Ellis, and S. Tummala, "Migration processing of spotlight SAR data," in *SPIE Algorithms for Synthetic Aperture Radar Imagery*, vol. 2230, Orlando, FL, 1994, pp. 25–35.

[8] J. Fortuny, E. Ohlmer, A. J. Sieber, P. Pasquali, C. Prati, and F. Rocca, "Validating SAR interferometry applications by using EMSL," in *Proc. IEEE Int. Geosci. Remote Sensing Symp. (IGARSS)*, vol. 2, Pasadena, CA, Aug. 1994, pp. 736–738.
[9] C. Yerkes and E. Webster, "Implementation of $w - k$ synthetic aperture radar imaging algorithm on a massively parallel supercomputer," in *Proc. SPIE*, vol. 2230, Orlando, FL, 1994, pp. 171–178.
[10] R. K. Raney, H. Runge, R. Bamler, I. G. Cumming, and F. H. Wong, "Precision SAR processing using chirp scaling," *IEEE Trans. Geosci. Remote Sensing*, vol. 32, pp. 786–799, July 1994.
[11] A. Broquetas, L. Jofre, and A. Cardama, "A near field spherical wave inverse synthetic aperture radar technique," in *Proc. IEEE Antennas Propagat. Soc. Int. Symp.*, vol. 2, Chicago, IL, July 1992, pp. 114–117.
[12] J. Fortuny, A. J. Sieber, J. Palau, and A. Broquetas, "QUICKSAR: A near field linear/inverse synthetic aperture radar processor," in *Proc. Progress Electromagn. Res. Symp.*. Nordwijk, The Netherlands, 1994.
[13] A. Broquetas, J. Palau, L. Jofre, and A. Cardama, "Spherical wave near-field imaging and radar cross-section measurement," *IEEE Trans. Antennas Propagat.*, vol. 46, no. 5, pp. 730–735, May 1998.
[14] J. Fortuny, "An efficient three dimensional near field ISAR algorithm using the method of stationary phase," *IEEE Trans. Aerosp. Electron. Syst.*, pp. 1261–1270, Oct. 1998.
[15] J. Fortuny and A. J. Sieber, "Fast algorithm for a near field synthetic aperture radar processor," *IEEE Trans. Antennas Propagat.*, vol. 41, pp. 1458–1460, Oct. 1994.
[16] K. Mayer, R. Marklein, K. J. Langenberg, and T. Kreutter, "Three-dimensional imaging system based on Fourier synthetic aperture focusing technique," *Ultrason.*, vol. 28, pp. 241–255, July 1990.
[17] K. J. Langenberg, M. Brandfaß, K. Mayer, T. Kreutter, A. Brüll, O. Fellinger, and D. Huo, "Principles of microwave imaging and inverse scattering," in *Proc. EARSel Adv. Remote Sensing Symp.*, vol. 2, Alpach, Austria, 1993, pp. 163–186.
[18] M. Fink, "Time reversal of ultrasonic fields—Part I: Basic principles," *IEEE Trans. Ultrason., Ferroelect., Freq. Contr.*, vol. 30, no. 5, pp. 555–566, 1992.
[19] F. Wu, J. L. Thomas, and M. Fink, "Time reversal of ultrasonic fields—Part II: Experimental results," *IEEE Trans. Ultrason., Ferroelect., Freq. Contr.*, vol. 30, no. 5, pp. 567–578, 1992.
[20] D. Cassereau and M. Fink, "Time reversal of ultrasonic fields—Part III: Theory of the closed time-reversal cavity," *IEEE Trans. Ultrason., Ferroelect., Freq. Contr.*, vol. 30, no. 5, pp. 579–592, 1992.
[21] A. Papoulis, *Systems and Transforms with Applications in Optics*. New York: McGraw-Hill, 1968.
[22] F. J. Harris, "On the use of windows for harmonic analysis with the discrete Fourier transform," *Proc. IEEE*, vol. 66, pp. 51–83, Jan. 1978.

Juan M. Lopez-Sanchez (S'94) was born in Alicante, Spain, in 1972. He received the Ing. degree in telecommunications engineering from the Polytechnic University of Valencia (UPV), Valencia, Spain, in 1996. He is currently working toward the Ph.D. degree at the same university.

From 1994 to 1997. he worked at the Communications Department, UPV, in numerical methods for electromagnetics, focusing on spectral techniques applied to antenna design and analysis and to propagation models. In 1998 he joined (with a predoctoral grant) the Joint Research Centre of the European Commission, Ispra, Italy. His main research interests include analytical and numerical models for multiple scattering problems, microwave remote sensing for inversion of biophysical parameters, polarimetric techniques, and SAR imaging algorithms.

Joaquim Fortuny-Guasch (S'93–M'96) was born in Tarragona, Spain, in 1964. He received the Ing. degree in telecommunications engineering from the Polytechnic University of Catalonia (UPC), Barcelona, Spain, in 1988.

From 1988 to 1989, he worked on the design of microwave circuits at Ka-band in the Antennas, Microwave, and Radar Group at the UPC. From 1990 to 1992 he worked as a Research Assistant in the RF Division, European Space Technology Centre, ESA, The Netherlands. Since 1993 he has been with the Joint Research Centre of the European Commission, Ispra, Italy. His research interests are in radar imaging, subsurface sensing, and numerical techniques in electromagnetics.